BRAIN
ORIGINAL ARTICLE

Network structure and transcriptomic vulnerability shape atrophy in frontotemporal dementia

Golia Shafiei,[1,†] Vincent Bazinet,[1,†] Mahsa Dadar,[1,2] Ana L. Manera,[1] D. Louis Collins,[1] Alain Dagher,[1] Barbara Borroni,[3] Raquel Sanchez-Valle,[4] Fermin Moreno,[5,6] Robert Laforce Jr,[7] Caroline Graff,[8,9] Matthis Synofzik,[10,11] Daniela Galimberti,[12,13] James B. Rowe,[14] Mario Masellis,[15] Maria Carmela Tartaglia,[16] Elizabeth Finger,[17] Rik Vandenberghe,[18,19,20] Alexandre de Mendonça,[21] Fabrizio Tagliavini,[22] Isabel Santana,[23,24] Chris Butler,[25,26] Alex Gerhard,[27,28] Adrian Danek,[29] Johannes Levin,[29,30,31] Markus Otto,[32] Sandro Sorbi,[33,34] Lize C. Jiskoot,[35] Harro Seelaar,[35] John C. van Swieten,[35] Jonathan D. Rohrer,[36] Bratislav Misic,[1,†] Simon Ducharme,[1,37,†] Frontotemporal Lobar Degeneration Neuroimaging Initiative (FTLDNI) and GENetic Frontotemporal dementia Initiative (GENFI)

[†]These authors contributed equally to this work.

Connections among brain regions allow pathological perturbations to spread from a single source region to multiple regions. Patterns of neurodegeneration in multiple diseases, including behavioural variant of frontotemporal dementia (bvFTD), resemble the large-scale functional systems, but how bvFTD-related atrophy patterns relate to structural network organization remains unknown. Here we investigate whether neurodegeneration patterns in sporadic and genetic bvFTD are conditioned by connectome architecture. Regional atrophy patterns were estimated in both genetic bvFTD (75 patients, 247 controls) and sporadic bvFTD (70 patients, 123 controls). First, we identified distributed atrophy patterns in bvFTD, mainly targeting areas associated with the limbic intrinsic network and insular cytoarchitectonic class. Regional atrophy was significantly correlated with atrophy of structurally- and functionally-connected neighbours, demonstrating that network structure shapes atrophy patterns. The anterior insula was identified as the predominant group epicentre of brain atrophy using data-driven and simulation-based methods, with some secondary regions in frontal ventromedial and antero-medial temporal areas. We found that FTD-related genes, namely *C9orf72* and *TARDBP*, confer local transcriptomic vulnerability to the disease, modulating the propagation of pathology through the connectome. Collectively, our results demonstrate that atrophy patterns in sporadic and genetic bvFTD are jointly shaped by global connectome architecture and local transcriptomic vulnerability, providing an explanation as to how heterogenous pathological entities can lead to the same clinical syndrome.

1   McConnell Brain Imaging Centre, Montreal Neurological Institute, McGill University, Montreal, QC, Canada
2   Radiology and Nuclear Medicine, Laval University, Quebec City, QC, Canada
3   Centre for Neurodegenerative Disorders, Department of Clinical and Experimental Sciences, University of Brescia, Brescia, Italy

4 Alzheimer's Disease and Other Cognitive Disorders Unit, Neurology Service, Hospital Clínic, Institut d'Investigacións Biomèdiques August Pi I Sunyer, University of Barcelona, Barcelona, Spain
5 Cognitive Disorders Unit, Department of Neurology, Donostia University Hospital, San Sebastian, Gipuzkoa, Spain
6 Neuroscience Area, Biodonostia Health Research Institute, San Sebastian, Gipuzkoa, Spain
7 Clinique Interdisciplinaire de Mémoire, Département des Sciences Neurologiques, CHU de Québec, and Faculté de Médecine, Université Laval, Quebec, QC, Canada
8 Department of Geriatric Medicine, Karolinska University Hospital-Huddinge, Stockholm, Sweden
9 Unit for Hereditary Dementias, Theme Aging, Karolinska University Hospital, Solna, Sweden
10 Department of Neurodegenerative Diseases, Hertie-Institute for Clinical Brain Research and Center of Neurology, University of Tübingen, Tübingen, Germany
11 Center for Neurodegenerative Diseases (DZNE), Tübingen, Germany
12 Fondazione IRCCS Ca' Granda Ospedale Maggiore Policlinico, Neurodegenerative Diseases Unit, Milan, Italy
13 Department of Biomedical, Surgical and Dental Sciences, University of Milan, Dino Ferrari Center, Milan, Italy
14 University of Cambridge, Department of Clinical Neurosciences, Cambridge University Hospitals NHS Trust, and MRC Cognition and Brain Sciences Unit, Cambridge, UK
15 Sunnybrook Health Sciences Centre, Sunnybrook Research Institute, University of Toronto, Toronto, ON, Canada
16 Toronto Western Hospital, Tanz Centre for Research in Neurodegenerative Disease, Toronto, ON, Canada
17 Department of Clinical Neurological Sciences, University of Western Ontario, London, ON, Canada
18 Laboratory for Cognitive Neurology, Department of Neurosciences, KU Leuven, Leuven, Belgium
19 Neurology Service, University Hospitals Leuven, Leuven, Belgium
20 Leuven Brain Institute, KU Leuven, Leuven, Belgium
21 Faculty of Medicine, University of Lisbon, Lisbon, Portugal
22 Fondazione Istituto di Ricovero e Cura a Carattere Scientifico Istituto Neurologico Carlo Besta, Milan, Italy
23 Neurology Department, Centro Hospitalar e Universitário de Coimbra, Coimbra, Portugal
24 Center for Neuroscience and Cell Biology, Faculty of Medicine, University of Coimbra, Coimbra, Portugal
25 Department of Clinical Neurology, University of Oxford, Oxford, UK
26 Department of Brain Sciences, Imperial College London, London, UK
27 Division of Neuroscience and Experimental Psychology, Faculty of Medicine, Biology and Health, University of Manchester, Manchester, UK
28 Department of Geriatric Medicine and Nuclear Medicine, University of Duisburg-Essen, Duisburg and Essen, Germany
29 Department of Neurology, Ludwig-Maximilians-Universität München, Munich, Germany
30 Clinical Research Unit, German Center for Neurodegenerative Diseases (DZNE), Munich, Germany
31 Munich Cluster of Systems Neurology (SyNergy), Munich, Germany
32 Department of Neurology, University Hospital Ulm, Ulm, Germany
33 Department of Neurofarba, University of Florence, Florence, Italy
34 IRCCS Fondazione Don Carlo Gnocchi, Florence, Italy
35 Department of Neurology, Erasmus University Medical Centre, Rotterdam, The Netherlands
36 Department of Neurodegenerative Disease, Dementia Research Centre, UCL Institute of Neurology, Queen Square, London, UK
37 Department of Psychiatry, Douglas Mental Health University Institute, McGill University, Montreal, QC, Canada

Correspondence to: Bratislav Misic
3801 Rue University
Webster 211, Montreal
QC H3A 2B4, Canada
E-mail: bratislav.misic@mcgill.ca

Introduction

Frontotemporal dementia (FTD) is one of the most common forms of early-onset dementia.[1,2] The behavioural variant of FTD (bvFTD), which presents with various combinations of behavioural (apathy, disinhibition, compulsions and stereotypies), personality (decreased empathy and sympathy, altered personal preferences) and cognitive (executive dysfunction and social cognitive deficits) changes, is the most common clinical variant of FTD.[2,3] Despite its distinctive clinical presentation, bvFTD is pathologically heterogenous, with the most common subtypes being related to the accumulation of hyperphosphorylated aggregates of either Tau or TDP-43.[4] This group of pathological proteinopathies causing FTD are classified under the frontotemporal lobar degeneration (FTLD) umbrella. Most cases are sporadic; however, around 20% are caused by an autosomal-dominant genetic mutation including hexanucleotide repeat expansions near *C9orf72*, *GRN* and *MAPT*, as the most common causative genes.[4]

FTLD pathology cause clinical bvFTD symptoms through their predominant localization in frontal and anterior temporal brain regions.[4] Clinically, this is reflected by progressive cortical atrophy, which is a crucial biomarker for the diagnosis.[5,6] While there is

major overlap in atrophy patterns between sporadic and genetic bvFTD, each genetic subtype has distinctive features, including antero-medial atrophy in *MAPT*, posterior frontal and parietal involvement in *GRN* and thalamic/cerebellar volume loss in *C9orf72*.[7] In recent years, there has been an interest to understand how heterogeneous pathological changes could lead to similar clinical and atrophy profiles.[8]

In early work based on functional MRI, it was hypothesized that atrophy in neurodegenerative diseases progresses predominantly along functional neural networks,[9] with the salience network being predominantly affected in bvFTD.[10,11] Within the salience network, the anterior insula was identified as the most likely disease epicentre,[9,11] a finding that was further supported by pathologic accumulation of tau or TDP-43 aggregates in fork cells and Von Economo neurons, which are specific to this region.[12] While the anterior insula clearly plays a significant role in the disease, other studies using data-driven methods on structural atrophy patterns revealed distinct morphological subtypes including two salience network-predominant subgroups (a frontal/temporal subtype and a frontal subtype), a semantic appraisal network-predominant group and a subcortical-predominant group.[13] This opens the possibility that there is not a single unique epicentre at the origin of all bvFTD cases.

Emerging theories emphasize that connectome architecture shapes the course and expression of multiple neurodegenerative diseases.[14–18] Misfolding of endogenous proteins and their subsequent trans-neuronal spread has been documented in FTLD, Alzheimer's disease, Parkinson's disease, Huntington's disease and amyotrophic lateral sclerosis.[9,19–26] Despite differences in origin and the proteins involved in each disease, the spread of the pathology appears to reflect brain network organization at the macroscale level. Namely, anatomical connectivity is thought to support the propagation of toxic protein aggregates, such that focal pathology can spread between connected neuronal populations and infiltrate distributed networks in the brain.

Two key questions remain unanswered about the spread of pathology in bvFTD. First, the spread of pathology is likely to occur via physical white matter connections, but the contribution of structural connectivity to atrophy progression has been less explored in bvFTD. Evidence for transneuronal spread of FTLD pathology is mostly based on extrapolation from functional imaging,[8,9] with some support from studies using animal models,[27] autopsy data[28] and prediction of atrophy patterns.[29] Although functional connectivity reflects the underlying structural connectivity patterns and is sometimes used as a proxy for structural connectivity if no such data is available, the two modalities capture fundamentally different features of brain network organization and are only moderately correlated with each other.[30] Second, the role of local vulnerability is poorly understood. It is possible that regional differences in molecular and cellular make-up render some nodes more or less vulnerable.[31–33] In particular, recent reports in other neurodegenerative diseases suggest that regional differences in gene expression may confer vulnerability, effectively guiding the pathological process through the network.[34–36] Altogether, we hypothesize that brain network architecture, in concert with local vulnerability conferred by expression of specific genes, shapes the spatial distribution of atrophy patterns in brain disorders, including FTD.[11,37]

In the present study, we tested a structural network-based atrophy propagation model in bvFTD across sporadic and genetic variants. Specifically, we tested the hypothesis that atrophy patterns in bvFTD reflect the underlying network organization and local transcriptomic vulnerability. First, we estimated cortical atrophy patterns as regional changes in tissue deformation in bvFTD patients. We then used structural and functional connectivity networks derived from an independent sample of healthy individuals to investigate whether regions that are connected to each other display similar atrophy patterns. Finally, we identified potential disease epicentres using a data-driven approach as well as a simulation-based approach that models the spread of atrophy across the brain network. We further explored the potential contribution of FTD-related genes to the propagation of atrophy.

Participants and methods

Participants

We retrieved data from subjects with bvFTD and cognitively normal controls (CNCs) from the Frontotemporal Lobar Degeneration Neuroimaging Initiative (FTLDNI) database, which contains T_1-weighted MRI scans matching each clinical visit (http://4rtni-ftldni.ini.usc.edu/). The inclusion criterium for bvFTD patients was a diagnosis of possible or probable bvFTD, according to the FTD consortium criteria,[3] resulting in 70 patients with bvFTD (mostly sporadic) and 123 CNCs available for analyses. Several patients had more than one scan; therefore, there was a total of 156 scans in the bvFTD group and 326 in the CNC group. We also accessed data from the third data freeze (12/2017) of the Genetic Frontotemporal Dementia Initiative 2 (GENFI2—http://genfi.org.uk/), which includes 23 centres in the UK, Europe and Canada.[38] GENFI2 participants included known symptomatic carriers of a pathogenic mutation in *C9orf72*, *GRN* or *MAPT* and their first-degree relatives, who are at risk of carrying a mutation, but do not show any symptoms (i.e. at-risk subjects). Healthy first-degree relatives, who were found to be non-carriers of a mutation, were considered CNCs. Since the aim of the present study was to study network propagation of atrophy in the bvFTD clinical phenotype, presymptomatic carriers and symptomatic carriers whose clinical diagnosis was other than bvFTD were excluded. This GENFI2 cohort included 75 patients with bvFTD and 247 CNCs. Demographic and clinical characteristics of these two cohorts are described in Table 1. Two-sample *t*-tests were conducted to examine demographic and clinical variables at baseline. Categorical variables were analysed using χ^2 analyses. Results are expressed as mean ± standard deviation (SD) and median (interquartile range) as appropriate.

MRI acquisition and processing

For the FTLDNI cohort, 3.0 T MRIs were acquired at three sites [T_1-weighted magnetization-prepared rapid gradient-echo imaging (MPRAGE), repetition time (TR) = 2 ms, echo time = 3 ms, inversion time = 900 ms, flip angle 9°, matrix 256 × 240, slice thickness 1 mm, voxel size 1 mm³]. For the GENFI2 sample, volumetric T_1-weighted MPRAGE MRI was obtained at multiple centres using the GENFI imaging protocol on either Siemens Trio 3 T, SiemensSkyra 3 T, Siemens 1.5 T, Phillips 3 T, General Electric (GE) 1.5 T or GE 3 T scanners. Scan protocols were designed at the outset of the study to ensure adequate matching between the scanners and image quality control.

All T_1-weighted scans were pre-processed through our longitudinal pipeline that included image denoising, intensity non-uniformity correction and image intensity normalization into range (0–100) using histogram matching.[39–42] The image processing tools used in this study were designed to process data from multisite studies to handle biases due to multi-site scanning, and they

Table 1 Demographic and clinical characteristics of the FTLDNI and GENFI2 samples

	FTLDNI $n = 193$			GENFI2 $n = 322$		
	CNCs $n = 123$	bvFTD $n = 70$	P-value	CNCs $n = 247$	bvFTD $n = 75$	P-value
Total number of scans	326	156		409	119	
Age mean (SD), years	63 ± 6	62 ± 6	0.36	48 ± 14	64 ± 8	<0.001
Males, n (%)	53(43%)	47(67%)	0.001	106(43%)	41(55%)	0.07
Education mean (SD), years	17.5 ± 1.9	15.6 ± 3.4	<0.001	13.9 ± 3.5	11.8 ± 4.03	<0.001
Estimated years of onset mean (SD), years	—	N/A	—	—	5.2 ± 5.7	—
Disease duration mean [min-max], years					5.1[3.5-8.2]	
MMSE score mean (SD)	29.4 ± 0.8	23.6 ± 4.9	<0.001	29.4 ± 1.1	21.9 ± 7.2	<0.001
FTLD-CDR score mean (SD)	0.04 ± 0.2	6.3 ± 3.3	<0.001	0.21 ± 0.7	9.7 ± 1.4	<0.001
Genetic group, n (%)						
C9orf72	—	—		—	39(52%)	
MAPT	—	—		—	17(22.7%)	
GRN	—	—		—	19(25.3%)	

CNCs in the GENFI2 cohort correspond to non-carrier first degree relative of a family member with a documented genetic mutation related to FTD. Genetic groups listed for CNCs in the GENFI2 cohort refer to mutation present in the family of these non-carrier subjects. Values are expressed as mean $\pm$ SD, median [interquartile range]. Data available is specified for each clinical variable as *n*, whereas N/A indicates data not available from the original databases.

have successfully been applied to a number of multi-site projects.[37,43–45] Each native T$_1$-weighted volume from each time point was linearly registered first to the subject-specific template, which was then registered to the ICBM152 template. All images were then non-linearly registered to the ICBM152 template using ANTs diffeomorphic registration pipeline.[46] The images were visually assessed by two experienced raters (M.D. and A.L.M.) to exclude cases with significant imaging artifacts (e.g. motion, incomplete field of view) or inaccurate linear/non-linear registrations. This visual quality control was completed blind to the diagnosis. Out of 1724 scans, only 43 (2.5%, 36 scans in GENFI2

and seven in FTLDNI) were rejected. This resulted in a total of 515 subjects that were included to perform cross-sectional morphometric analyses.

Deformation-based morphometry analyses

Deformation-based morphometry (DBM)[47,48] analysis was performed using Montreal Neurological Institute (MNI) MINC tools.[49] The local deformations, obtained from the non-linear transformations mapping the MNI-ICBM152-2009c template to the subject's MRI, encode the local tissue volume difference between the MNI average template and subject's brain. The determinant of the Jacobian of the deformation field is measured at each voxel. Determinant values >1.0 indicate that the local volume in the subject is larger than the average template (e.g. ventricular or sulci enlargement in the case of FTD). Determinant values <1.0 indicate that the local volume in the subject is smaller than the template. The latter is often interpreted as tissue atrophy, despite the use of only cross-sectional data. DBM was used to assess voxel-wise cross-sectional group-related volumetric differences. To obtain a voxel-wise map reflecting the patterns of difference between bvFTD and CNCs, the following mixed effects model was applied on a voxel-by-voxel basis, separately for each dataset:

$$DBM \sim 1 + Dx + AGE + SEX + (1/SITE) \tag{1}$$

The mixed effects model included 'age' as a continuous fixed variable and 'diagnosis (Dx)' and 'sex' as fixed categorical variables. 'Site' was included as a categorical random variable. The variable

of interest was 'diagnosis', reflecting the brain regions that were significantly different between bvFTD and CNCs, controlling for age and sex. Statistical *t*-maps were extracted from the model and used for the rest of the analyses throughout the manuscript. Finally, the *t*-statistics were multiplied by −1, such that higher positive values correspond to higher atrophy and negative values correspond to volume expansion in patients.

Anatomical parcellation

Statistical *t*-maps obtained through DBM analysis and mixed effects models were parcellated into 219 and 1000 approximately equally sized cortical regions or parcels using the Cammoun atlas,[50] a multiresolution extension of the anatomical Desikan–Killiany atlas.[51] We refer to 219 and 1000 parcellation resolutions as low and high parcellation resolutions, respectively. The parcel-wise *t*-statistics (i.e. atrophy) were estimated as the mean *t*-statistic of all the voxels that were assigned to that parcel according to the atlas. We repeated all the analyses at both parcellation resolutions to ensure that results are replicable across multiple spatial scales.

Structural and functional network reconstruction

Connection patterns from healthy individuals are used to represent the architecture of brain networks for the distributed atrophy patterns that are observed in bvFTD patients. Structural and functional connectivity data of 70 healthy individuals (mean age 28.8 ± 9.1 years) were obtained from a publicly available dataset.[52] Details about data acquisition parameters and preprocessing analysis are available in Griffa *et al.*[52] Briefly, the participants were scanned in a 3 T MRI scanner (Trio, Siemens Medical) using a 32-channel head-coil. The session protocol included: (i) an MPRAGE sequence sensitive to white/grey matter contrast (1-mm in-plane resolution, 1.2-mm slice thickness); (ii) a diffusion spectrum imaging (DSI) sequence (128 diffusion-weighted volumes and a single b_0 volume, maximum *b*-value 8000 s/mm^2, $2.2 \times 2.2 \times 3.0$ mm voxel size); and (iii) a gradient echo echo-planar imaging sequence sensitive to blood–oxygen-level-dependent (BOLD) contrast (3.3-mm in-plane resolution and slice thickness with a 0.3-mm gap, TR 1920 ms, resulting in 280 images per participant). DSI data and deterministic streamline tractography were used to construct structural connectivity networks for each healthy

individual. Each pair-wise structural connection was weighted by the log-transform of the fibre density. Individual structural connectivity networks were parcellated into the low and high parcellation resolutions using the Cammoun atlas described before. Resting-state functional MRI data collected in the same healthy individuals (with eyes open) were used to construct functional connectivity networks. The preprocessed resting-state functional MRI time series was also parcellated using both the low and high resolution versions of the Cammoun atlas and were correlated to estimate functional connectivity between pairs of brain regions using Pearson correlation coefficients. Finally, a consensus group-average structural connectivity preserving the edge length distributions in individual networks[53–55] was constructed and a group-average functional connectivity was estimated as the mean pairwise connectivity across individuals.

Network atrophy

Group-average structural and functional connectivity networks were used to estimate average atrophy values of neighbours of each brain region.[56] Briefly, neighbours of a given brain region were defined as regions connected to it with a structural connection for both structurally- and functionally-defined neighbours. The structurally-connected neighbour atrophy value of each brain region was then estimated as the average weighted atrophy values of all the neighbours of that region:

$$A_i = \frac{1}{N_i} \sum_{j=1}^{N_i} a_j \times SC_{ij} \, , \ j \neq i \qquad (2)$$

where A_i is the average neighbour atrophy value of brain region or node i, a_j is atrophy of the j-th neighbour of node i, SC_{ij} is the strength of structural connection between nodes i and j, and N_i is the total number of neighbours that are connected to node i with a structural connection (i.e. node degree). Normalization by term N_i ensures that the estimated neighbour atrophy value is independent from the node degree. The neighbour atrophy estimation excludes self-connections ($j \neq i$). The functionally-connected neighbour atrophy values were estimated using the same equation as above, with the exception that regional atrophy values were weighted by the strength of functional connections between nodes i and j (FC_{ij}):

$$A_i = \frac{1}{N_i} \sum_{j=1}^{N_i} a_j \times FC_{ij} \, , \ j \neq i \qquad (3)$$

For both structurally- and functionally-defined neighbour atrophy estimates, neighbours were defined as nodes that were structurally connected to the node under consideration. Altogether, a single neighbour atrophy value was estimated for each region. We used Pearson correlation coefficients to assess the relationship between node atrophy and mean neighbour atrophy for structurally- and functionally-defined neighbours, separately (Fig. 2A).

Data-driven epicentre analysis

To identify potential disease epicentres, we hypothesized that an epicentre would be a node with high atrophy that is also connected to highly atrophied neighbours, compared with a high atrophy node with healthy neighbours or a healthy node with atrophied neighbours. Using a data-driven approach,[56,57] we first ranked the nodes based on their estimated regional atrophy values. We also ranked the nodes based on the average atrophy values of their neighbours

in a separate list. We then calculated the average ranking of each node in the two lists and identified nodes that were highly ranked in both lists (i.e. nodes with both high local and neighbourhood average rankings) as the potential epicentres (Fig. 2B).

Agent-based spreading model

Simulation-based epicentre analysis

To investigate the trans-neuronal spread hypothesis, we simulated the spread of pathology on the left hemisphere of the low-resolution weighted consensus structural connectivity network (111 regions) using a Susceptible-Infected-Removed (SIR) agent-based model.[34] Briefly, the model consists of simulating the misfolding of normal proteins in the cortex and their trans-neuronal spreading through the structural connections between brain regions. The accumulation of pathology, which act as pathogenic agents, then leads to the atrophy of the afflicted regions. Importantly, this model incorporates synthesis and clearance rates, which can vary heterogeneously across brain regions. More details about the model's main equations can be found in the Supplementary material. To explore the likelihood that a brain region acts as an epicentre of this spreading process, we first used baseline clearance and synthesis rates for all regions. We simulated the spread of pathology and the resulting atrophy using, one at a time, each individual brain region as the seed of the process. For each seed region, and at each time point, we then computed the Pearson correlation between the simulated and empirical patterns of atrophy.

Gene expression

To investigate the potential role of gene expression in shaping the modelled patterns of atrophy, we accessed the Allen Human Brain Atlas (AHBA; http://human.brain-map.org/),[58] which provides regional microarray expression data from six post-mortem brains (one female, ages 24–57 years, 42.5 ± 13.38 years). We generated vectors storing gene expression scores for each of the 111 regional parcels of the left hemisphere. These vectors were then incorporated into the SIR model to regulate the synthesis and clearance rate of each region, such that a greater expression score entailed greater synthesis and clearance rates More specifically, our analyses focused on four vectors of gene expression associated with genes that have been linked previously to bvFTD, namely *MAPT*, *GRN*, *C9orf72* and *TARDBP*. Given that subjects were selected based on their clinical phenotype (bvFTD) rather than on a specific pathological subtype or genetic mutation, we explored the potential role of the expression of all four genes for both synthesis and clearance. Our objective was to identify potentially new mechanistic processes underlying the spreading of atrophy, particularly in sporadic bvFTD, where we do not have adequate knowledge of the contribution of genes related to the various proteinopathies. In complementary experiments, we also used the first principal component of the full 'genes × brain regions' matrix of gene expression. This component captures the principal axis of transcriptional variation across the human cortex.[59]

The AHBA data were preprocessed and mapped to the parcellated brain regions using the abagen toolbox (https://github.com/rmarkello/abagen).[60] During pre-processing, we first updated the MNI coordinates of tissue samples to those generated via non-linear alignment to the ICBM152 template anatomy (https://github.com/chrisgorgo/alleninf). We also reannotated the microarray probe information for all genes using data provided by

Arnatkevičiūtė and colleagues.[61] We then filtered the probes by only retaining those that have a proportion of signal to noise ratio greater than 0.5. When multiple probes indexed the expression of the same gene, we selected the one with the most consistent pattern of regional variation across donors. Samples were then assigned to individual regions in the Cammoun atlas. If a sample was not found directly within a parcel, the nearest sample, up to a 2 mm-distance, was selected. If no samples were found within 2 mm of the parcel, we used the sample closest to the centroid of the empty parcel across all donors. To reduce the potential for mis-assignment, sample-to-region matching was constrained by hemisphere and gross structural divisions (i.e. cortex, subcortex/brainstem, and cerebellum, such that e.g. a sample in the left cortex could only be assigned to an atlas parcel in the left cortex). All tissue samples not assigned to a brain region in the provided atlas were discarded. Tissue sample expression scores were then normalized across genes using a scaled robust sigmoid function[62] and were re-scaled to a unit interval. Expression scores were also normalized across tissue samples using the same procedure. We then aggregated the microarray samples belonging to the same regions by computing the mean expression across samples for individual parcels for each donor. Regional expression profiles were finally averaged across donors.

Null models

To assess the statistical significance of the node-neighbour relationships and the epicentre analysis, we used a spatial autocorrelation preserving null model (i.e. 'spin tests'[63,64]). We first used the Connectome Mapper toolkit[65] (https://github.com/LTS5/cmp) to generate a surface-based representation of the Cammoun atlas (both low and high resolution) on the Freesurfer fsaverage surface. We then defined the spatial coordinates of each parcel by selecting the vertex on the spherical projection of the generated fsaverage surface that was closest to the centre of mass of the parcel.[56,57] Finally, we used the resulting parcel spatial coordinates to generate null models of brain maps (e.g. atrophy maps, epicentre rankings) by randomly rotating the maps and reassigning node values with the values of closest parcels. The rotations were first applied to one hemisphere and the mirrored rotations were used for the other hemisphere. This procedure was repeated 10 000 times to generate a null distribution of brain maps with preserved spatial autocorrelation.

To ensure the specificity of our transcriptomic results, we relied on a second spatial autocorrelation-preserving null model. This model was proposed by Burt and colleagues[66] and can be implemented using the brainSMASH python toolbox (https://github.com/murraylab/brainsmash). First, the empirical brain map is randomly permuted. Then, this permuted brain map is spatially smoothed and re-scaled to re-introduce the spatial autocorrelation (SA) of the empirical brain map. The smoothing process is achieved via the following transformation:

$$y = |\beta|^{1/2}x + |\alpha|^{1/2}z \tag{4}$$

where y is the surrogate map, x is the permuted data and z is a vector of random gaussian noise. The α and β parameters are estimated via a least-square optimization between variograms of the original and permuted data. By maximizing the fit between the variograms of the original and permuted data, we ensure that the SA of the surrogate map matches the SA of the empirical map.

To ensure that the observed correlation between the empirical and simulated atrophy map from the agent-based model is explained by the topological organization of the structural connection between brain regions and not solely by the spatial embedding of brain regions, we generated surrogate networks that preserve the geometry of the structural connectome. The edges of the consensus network were first binned according to inter-regional Euclidean distance. Within each length bin, pairs of edges were then selected at random and swapped.[67] This procedure was repeated 500 times, generating a population of rewired structural networks that preserve the degree sequence of the original network and that approximately preserve the edge length distribution (i.e. wiring cost) of the empirical network.

Data availability

Data used in this study are part of FTLDNI and GENFI databases and de-identified data can be accessed upon request at http://4rtni-ftldni.ini.usc.edu/ and http://genfi.org.uk/, respectively, after agreeing to their corresponding data terms.

Results

Demographics

Table 1 compares demographic and clinical variables between bvFTD and CNCs across the two research databases. Subjects with bvFTD were on average older than CNCs in the GENFI2 cohort but not in FTLDNI. As expected, significantly lower average MMSE and higher FTLD-CDR scores were observed in symptomatic subjects compared with healthy controls.

Distribution of atrophy and resting state networks and cytoarchitectonic classes

We used a linear mixed effects model to obtain a group-level, bvFTD-related atrophy map, controlling for age, sex and acquisition site. The voxel-level and parcellated atrophy maps are depicted in Supplementary Fig. 1A and B. To assess whether distributed atrophy patterns are more pronounced in specific brain systems, we used two brain system definitions (Fig. 1): (i) intrinsic functional networks defined by Yeo and colleagues[68]; and (ii) a cytoarchitectonic classification of human cortex based on the classic von Economo atlas.[69–72] Nodes were first stratified according to their network assignments based on the Yeo networks and von Economo classes. We then calculated the mean atrophy values for each intrinsic network (Fig. 1, left) and cytoarchitectonic class (Fig. 1, right) for the FTLDNI (Fig. 1A) and GENFI (Fig. 1B) datasets, separately. To assess the statistical significance of network atrophy values, we compared the empirical values to a distribution of means calculated from a set of spatial autocorrelation-preserving null models (i.e. 'spin tests'[63,64]; see the 'Materials and methods' section for more details on the null model). Specifically, network labels were randomly rotated while preserving the spatial autocorrelation and the mean network atrophy values were calculated for each rotation (10 000 repetitions; two-tailed test).

The observed mean network atrophy and the corresponding null distribution of means are depicted for each intrinsic network and cytoarchitectonic class in Fig. 1. The anatomical distributions of intrinsic networks and cytoarchitectonic classes are depicted in Fig. 1 (bottom row). Note the difference in the definition of 'limbic' system between the intrinsic networks and cytoarchitectonic classes. The intrinsic limbic network mainly consists of the
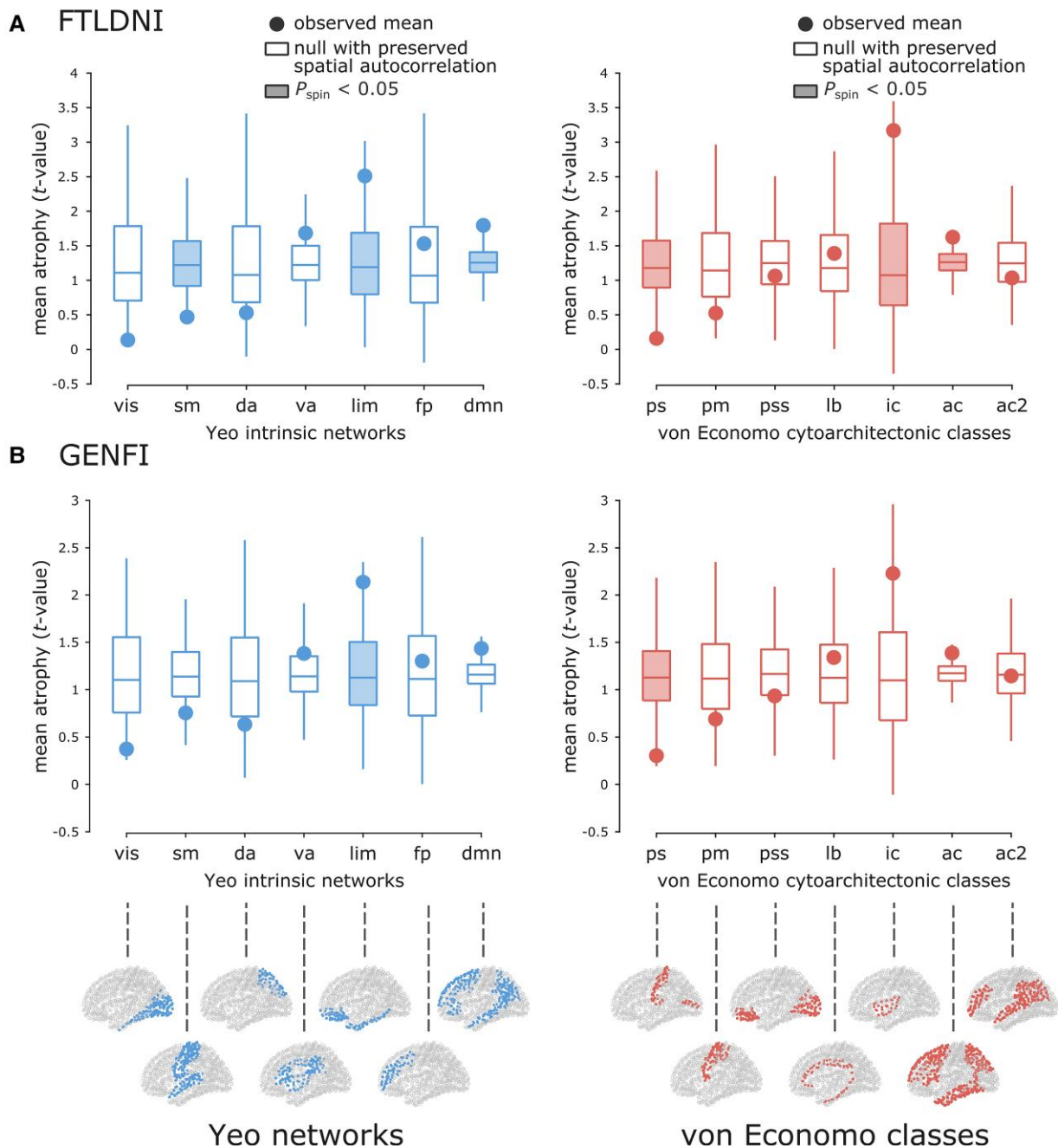
Figure 1 Atrophy patterns in intrinsic networks and cytoarchitectonic classes. Mean network atrophy (i.e. *t*-value) was calculated for Yeo intrinsic functional networks[68] (*left*) and von Economo cytoarchitectonic classes[69–72] (*right*). Higher *t*-values correspond to greater atrophy. The observed mean atrophy values are shown by filled circles for each intrinsic network and cytoarchitectonic class. Network labels are then randomly permuted using 10 000 rotations from spin tests, preserving the spatial autocorrelation in the data. The null distributions of means from spin tests are depicted using box plots for intrinsic networks and cytoarchitectonic classes for both (**A**) FTLDNI and (**B**) GENFI datasets (10 000 repetitions; two-tailed test). The bottom row displays the location of intrinsic networks (*left*) and cytoarchitectonic classes (*right*) on the cortex. List of Yeo networks: visual (vis), somatomotor (sm), dorsal attention (da), ventral attention (va), limbic (lim), frontoparietal (fp), default mode (dmn). List of von Economo classes: primary sensory cortex (ps), primary motor cortex (pm), primary/secondary sensory cortex (pss), limbic (lb), insular cortex (ic), association cortex (ac, ac2).

temporal poles and orbitofrontal cortex, whereas the cytoarchitectonic limbic class mainly includes the cingulum. In terms of intrinsic networks, limbic and default mode intrinsic networks were the most affected (i.e. higher than expected atrophy) with relative preservation of somatomotor and visual intrinsic networks (i.e. lower than expected atrophy). In terms of cytoarchitectonic classes, the insular and association cytoarchitectonic classes displayed greater atrophy compared to nulls, with lower atrophy in primary sensory cytoarchitectonic classes. While there are marginal variations in statistical significance of the findings, the overall trend of network atrophy patterns is consistent across the two datasets.
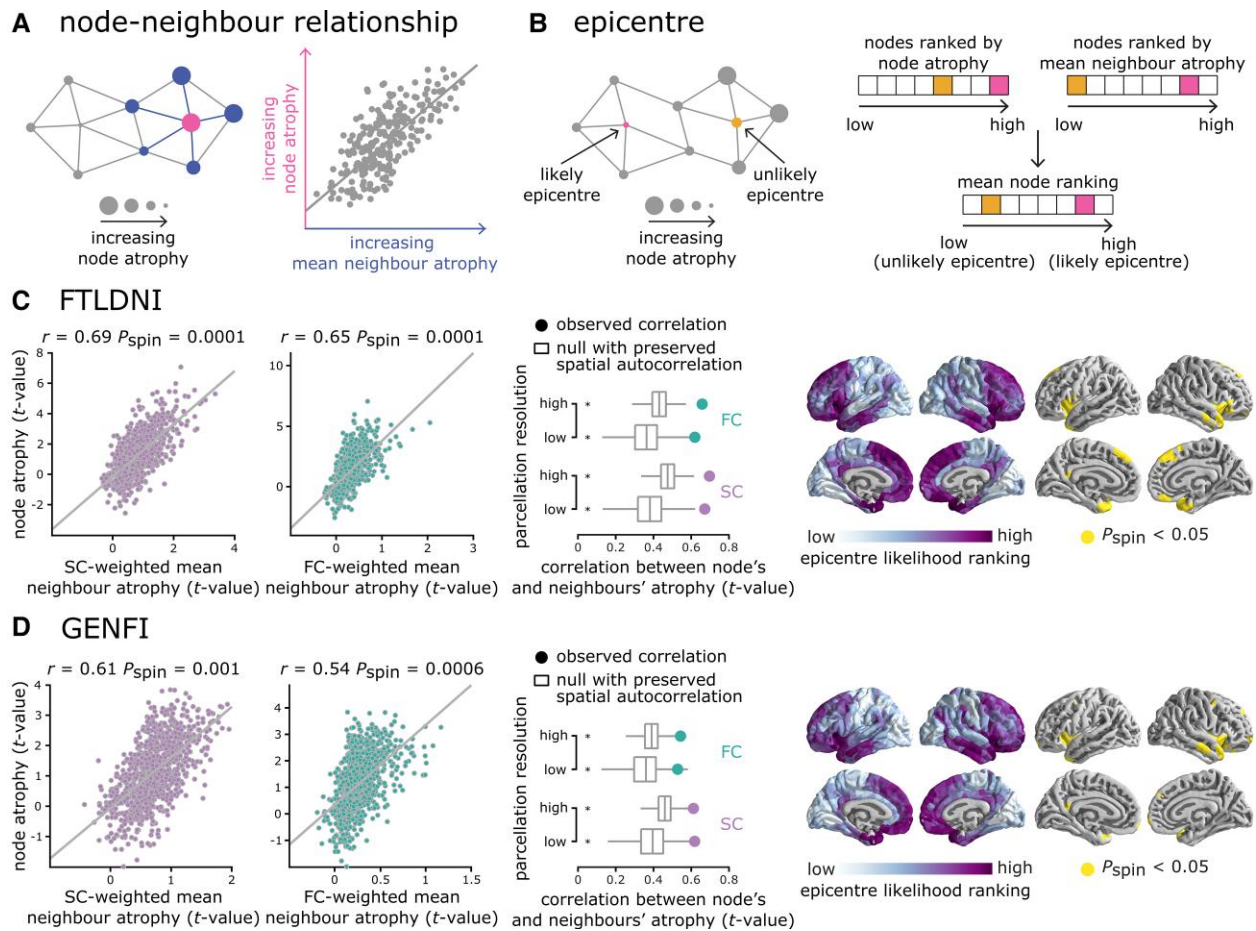
Figure 2 Network-dependent atrophy. (**A**) Atrophy of a node, estimated by *t*-values, was correlated with the mean atrophy of its connected neighbours to examine whether the distributed atrophy patterns in bvFTD reflect the underlying network organization. (**B**) If atrophy of a node is related to the atrophy of its connected neighbours (**A**), a node with high atrophy whose neighbours are also highly atrophied would be more likely to be a potential disease epicentre, compared with a high atrophy node with healthy neighbours. To quantify the epicentre likelihood across the cortex, the nodes were first ranked based on their atrophy values and their neighbours' atrophy values. Epicentre likelihood ranking of each node was then defined as its mean ranking in the two lists. (**C** and **D**) *Left*: Node atrophy value was correlated with the mean atrophy value of its structurally- and functionally-weighted neighbours (SC and FC) for FTLDNI (**C**) and GENFI (**D**) datasets. Scatter plots show the correlation for high parcellation resolution. *Middle*: The observed correlation values (depicted by filled circles) were compared to a set of correlations obtained from 10 000 spin tests (depicted by box plots). Asterisks denote statistical significance ($P_{spin} < 0.05$, two-tailed). The association between node and neighbour atrophy was consistent across resolutions and significantly greater in empirical networks compared to null networks in both datasets. *Right*: Epicentre likelihood rankings are depicted across the cortex. The most likely epicentres with high significant rankings are regions that are mainly located at the bilateral anterior insular cortex and temporal lobes (10 000 spin tests).

Relationship between atrophy maps and connectivity

We next investigated whether atrophy patterns in bvFTD are conditioned by network organization, such that connected regions display similar atrophy patterns. Specifically, we assessed whether the connectivity profile of a node can predict the atrophy of its neighbours by investigating the relationship between node and neighbour atrophy values (Fig. 2A). Structural and functional connectivity (SC and FC) networks (Supplementary Fig. 1C), derived from an independent sample of 70 healthy participants,[52] were used to estimate mean neighbour atrophy value for each region. The relationship between node and neighbour atrophy was then examined by correlating the mean neighbour atrophy with nodal atrophy (Fig. 2C and D). Regional atrophy was significantly correlated with the mean atrophy of its connected neighbours in both datasets. Fig. 2C (left panel) shows the results for FTLDNI dataset

(high resolution parcellation: $r = 0.69$, $P_{spin} = 0.0001$ and $r = 0.65$, $P_{spin} = 0.0001$, for SC- and FC-defined neighbours, respectively) and Fig. 2D (left panel) shows the results for GENFI dataset (high resolution parcellation: $r = 0.61$, $P_{spin} = 0.001$ and $r = 0.54$, $P_{spin} = 0.0006$, for SC- and FC-defined neighbours, respectively). These correlations are significantly greater when considering connected versus not-connected neighbours, across datasets and resolutions (Supplementary Table 1).

To assess whether the relationship between node and neighbour atrophy is specifically driven by network topology rather than spatial autocorrelation, we used a spatial autocorrelation-preserving null model to construct a null distribution of node-neighbour correlations.[63] Fig. 2C and D (middle panel) display the observed correlation between node and neighbour atrophy along with the corresponding null distribution of correlations for both datasets. We also repeated all analyses at a lower parcellation resolution to ensure that the findings are robust to how network

nodes are defined. The relationship between node and neighbour atrophy was consistent across resolutions and significantly greater in empirical networks compared to null networks in both datasets (Fig. 2C and D; $P_{spin} < 0.05$, two-tailed tests). The results were consistent when the binarized structural connectivity network was used to defined SC-defined neighbours (Supplementary Fig. 2).

Data-driven epicentres analysis

Given that the distribution of atrophy patterns reflects structural and functional network organization, we next investigated whether there are brain regions that may act as potential epicentres for bvFTD. We define an epicentre as a high atrophy node that is connected to high atrophy neighbours (Fig. 2B). Nodes were ranked based on their atrophy and their neighbours' mean atrophy values. Epicentre likelihood ranking was then estimated as the mean node ranking across the two lists. Fig. 2C and D (right) show the epicentre likelihood rankings on the cortex for FTLDNI (Fig. 2C) and GENFI (Fig. 2D) datasets, where the highly ranked regions are associated with insular cortex, ventromedial cortex and antero-medial temporal areas. Empirical epicentre likelihood rankings were then compared with rankings estimated from spatial autocorrelation-preserving null models (10 000 spin tests[63]). Several regions were identified as potential epicentres including the anterior insular cortex bilaterally, but also areas in the anterior temporal poles, in addition to ventromedial and dorsomedial areas. The results were consistent when binarized structural connectivity network was used to define SC-defined neighbours (Supplementary Fig. 2).

Dynamic spreading model

Next, we used an SIR model to explore how the brain's structural connectivity shapes the progressive spread of FTLD changes. This model has previously been used to study Parkinson's disease-related atrophy[34] and works by simulating the misfolding of normal proteins in the cortex and their trans-neuronal spread through the structural connections between brain regions. The accumulation of pathology, acting as pathogenic agents, leads to the atrophy of the afflicted regions (Fig. 3A). Epicentres are defined as those regions in which misfolded proteins are introduced. We tested which is the most likely epicentre for the observed empirical patterns of atrophy by running the model and initiating the spread in each region. As the misfolded agents spread through the network, we measured the Pearson correlation between the simulated and empirical (FTLDNI) patterns of atrophy (Fig. 3B, left). We then define a region's r_{max} as the largest correlation value observed across all values of t when it is used as the epicentre of the spreading process. Regions that have large r_{max} scores are the most likely epicentres. The three nodes with the largest r_{max} are located in the insular, superior-frontal and lateral orbito-frontal cortex. For these three potential epicentres, the r_{max} is greater when considering directly-connected neighbours than when considering non-connected nodes (Supplementary Fig. 3).

An important factor that can influence the probability that a brain region is identified as the epicentre of an atrophy pattern is its spatial location in the brain. To isolate the role of structural connectivity, we compared these r_{max} scores to those obtained by simulating the spread of pathology in rewired networks that preserve the density, degree sequence and wiring cost of the empirical structural network (Fig. 3B, right). We found that the fit obtained by initiating the spread in the insular region of the empirical network

was significantly larger than the fit obtained in the rewired networks ($r = 0.601$, $P < 0.002$). We also found that it was larger than the fit obtained by replacing the structural connectivity matrix in our model with matrices of either Euclidean or geometric distances between nodes (Supplementary Fig. 4A). In other words, the fit observed by seeding the insula was significantly larger than what would have been expected from its degree and spatial position alone and can be attributed to its embedding in the global topology of the network. This result suggested that the topology of the structural connectome plays a significant role in shaping patterns of simulated atrophy that have a high correspondence with the empirical atrophy.

More generally, by looking at the topographic distribution of r_{max} scores, we found that the brain regions that showed the largest fits were located in the insular, medial prefrontal and anterior temporal cortices (Fig. 3C). These results were in accordance with our finding that these regions have large epicentre likelihood rankings. Fig. 3D shows the empirical pattern of atrophy for the FTLDNI dataset. This pattern is compared to the simulated pattern of atrophy producing the maximal fit. This largest fit was obtained by seeding the insula and was measured at $t = 4410$. We found a significant relationship between the two distributions ($r = 0.60$, $P = 0.0013$). Results are presented for the FTLDNI dataset, but similar results were found in the GENFI dataset (Supplementary Fig. 5). Up to this point, we focused on group effects because deformation-based morphometry is a technique mainly intended to detect population-level differences in brain structure. To better understand patient heterogeneity, we considered genetic subtypes in GENFI. We stratified the GENFI cohort into *C9orf72*, *GRN* and *MAPT* mutation carriers and repeated the main analyses separately for each genetic group. Supplementary Fig. 6A–C shows the three main findings for each genetic group separately. We found a significant network spreading effect in each group. In addition, both the data-driven and simulation-based analysis identified frontal, temporal and insular epicentres in *C9orf72* and *MAPT* carriers, with more pronounced involvement of the antero-medial temporal poles in *MAPT* as well as frontal and lateral parietal regions in *GRN* carriers, consistent with previous research.[7]

Contribution of gene expression to network spreading

Given the contribution of genetic variants to bvFTD,[73] we next assessed whether the incorporation of gene expression information into the SIR model can enhance the fits. We used regional microarray expression data from the AHBA[58] to generate vectors of gene expression for four genes that have been previously associated with bvFTD: *MAPT*, *GRN*, *C9orf72* and *TARDBP*.[4] Figure 4A shows their topographic distributions. We used this genetic information to set regional heterogeneity for the clearance and synthesis of proteins in the model. We used the insula as the seed region of the spreading process as it is the region that showed the largest fit to the empirical data.

For both the FTLDNI (Fig. 4B) and GENFI (Fig. 4C) datasets, we measured the r_{max} scores obtained by incorporating regional expression for each of the four genes. With *MAPT*, *GRN*, *C9orf72* and *TARDBP*, we obtained correlation scores of $r_{max} = 0.42$, $r_{max} = 0.44$, $r_{max} = 0.61$ and $r_{max} = 0.71$ for the FTLDNI dataset and $r_{max} = 0.28$, $r_{max} = 0.30$, $r_{max} = 0.58$ and $r_{max} = 0.68$ for the GENFI dataset. We found that adding regional heterogeneity for synthesis and clearance using expression of *C9orf72* and *TARDBP* increased model fit, while the incorporation of information regarding the regional
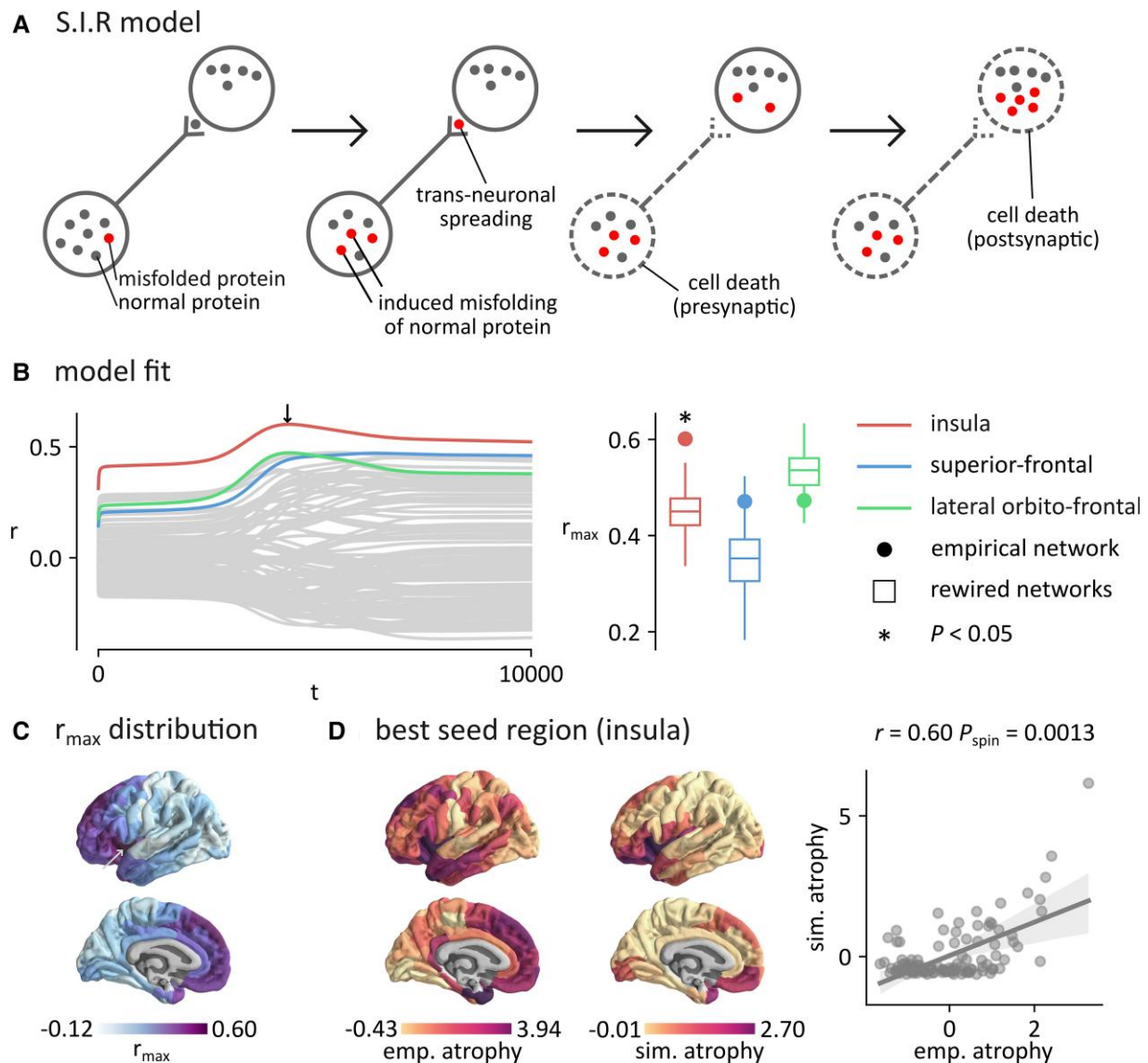
Figure 3 Agent-based modelling. (A) The SIR model simulates the spread of pathology in the brain. Proteins propagate via the structural connections between brain regions and induce atrophy, both pre- and post-synaptically. **(B)** *Left*: The spreading process was initiated in every brain region and the correlation between the simulated and empirical patterns of atrophy was computed. The three largest correlations were obtained by seeding regions of the insula ($r_{max} = 0.601$), the superior-frontal cortex ($r_{max} = 0.473$) and lateral orbito-frontal cortex ($r_{max} = 0.471$). *Right*: To control for the potential effect of a brain region's spatial embedding, r_{max} values were compared to r_{max} correlations obtained using rewired networks that preserve the wiring-cost of the empirical structural network. Asterisks denote statistical significance ($P < 0.05$, two-tailed). The r_{max} computed by seeding the insula of the empirical network ($r_{max} = 0.60$) was significantly larger than the r_{max} computed by seeding the insula of the rewired networks ($P < 0.002$). **(C)** The largest fit (r_{max}) obtained by seeding each brain region is shown on the surface of the brain. Larger values of r_{max} were generally obtained by seeding insular and prefrontal regions. **(D)** *Left*: Empirical pattern of atrophy (FTLDNI). *Middle*: Simulated pattern of atrophy producing the maximal fit. This pattern of atrophy was obtained with the insula as the seed, and at $t = 4410$ (see the arrow in **B**). *Right*: Scatter plot of the relationship between standardized empirical and simulated patterns of atrophy ($r = 0.60$, $P = 0.0013$).

expression of *GRN* and *MAPT* decreased model fit. To investigate the significance of the findings, we spun the vectors of gene expression 10 000 times to generate spatially auto-correlated null distributions of r_{max} scores that we compared to the empirical results. We found that the scores obtained with *C9orf72* and *TARDBP* were significantly larger than those obtained with permuted gene expression vectors ($P = 0.014$ and $P < 0.0001$, respectively, for the FTLDNI dataset, and $P < 0.0001$, for both genes, for the GENFI dataset). The scores obtained with *C9orf72* and *TARDBP* were also significantly larger than those obtained with spatially auto-correlated distributions of gene expression generated using a variogram-based method

(Supplementary Fig. 7). These results suggested that *C9orf72* and *TARDBP* may play a significant role in driving the spatial patterning of the empirical atrophy.

To investigate the relationship between gene expression and the brain's structural connectivity, we compared the fits to those obtained using rewired networks preserving the wiring-cost of the empirical network. For *C9orf72*, we found that the fits obtained using the empirical networks were significantly larger than the fits obtained using rewired null networks for both FTLDNI ($P < 0.002$) and GENFI ($P < 0.002$). The fits obtained with the empirical connectome were also greater than the fits obtained by replacing the
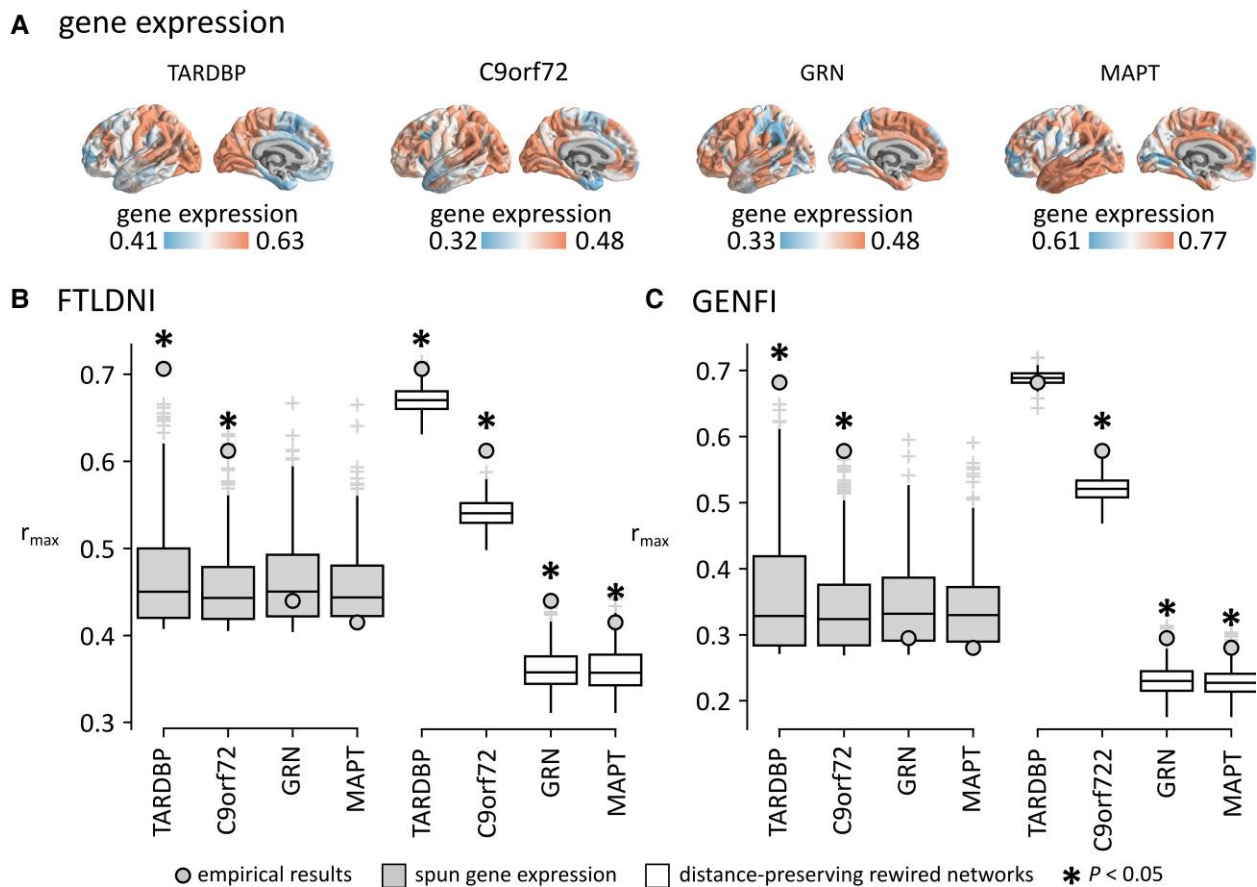
A gene expression

B FTLDNI

C GENFI

○ empirical results   ▪ spun gene expression   □ distance-preserving rewired networks   ＊ $P < 0.05$

Figure 4 Contribution of gene expression. (**A**) Vectors of regional gene expression were generated for four genes that have been associated with bvFTD: TARDBP, C9orf72, GRN and MAPT. These vectors of gene expression were incorporated into the SIR model. The correlations between empirical atrophy and simulated atrophy, with the insula selected as the seed of the simulated spreading process, were then computed for the FTLDNI dataset (**B**) and for the GENFI dataset (**C**). The maximal correlation scores (r_{max}) obtained for each gene were compared to the maximal correlation scores (r_{max}) obtained with spun distributions of gene expression vectors (left box plots). Asterisks denote statistical significance ($P < 0.05$, two-tailed). For both datasets, we find that the r_{max} scores obtained by incorporating information about the expression of C9orf72 and TARDBP were significantly larger than those obtained with permuted gene expression vectors. The maximal correlations were also compared to the maximal correlation scores obtained in distance-preserving rewired networks (*right* box plots).

structural connectivity matrix in the SIR model with matrices of either Euclidean or geometric distances between nodes (Supplementary Fig. 4B). For *TARDBP*, we found that the fits obtained using the empirical networks were significantly larger than the fits obtained using rewired nulls for FTLDNI ($P = 0.014$) but not for GENFI ($P = 0.508$). Similarly, the fits obtained with the empirical connectome were greater than the fits obtained by replacing it with matrices of Euclidean or geometric distances between nodes for the FTLDNI dataset but not the GENFI dataset (Supplementary Fig. 4B). Altogether, these results demonstrated that the topology of the structural connectome has a positive influence on the increase in model fit observed when incorporating either *TARDBP* or *C9orf72* into the SIR model, more so than would the spatial distances between nodes. For *TARDBP*, this influence was observed when trying to fit our model to patterns of atrophy associated to both sporadic and genetic bvFTD, while for *C9orf72*, this influence was only observed when trying to fit our models to patterns of atrophy associated to sporadic bvFTD. In other words, our investigations suggested that *C9orf72* and *TARDBP* expression can influence pathogenic spreading processes unfolding on the structural connectome. Interestingly, both *TARDBP* ($r = 0.83$) and *C9orf72* ($r = 0.61$) are strongly correlated to the principal axis of transcriptional variation across the human cortex (gene PC1[59]), which also enhances the fit of the SIR

model when used to incorporate regional heterogeneity (Supplementary Fig. 8). However, contrary to *TARDBP* and *C9orf72*, this increased fit was not significantly larger than the fits obtained using rewired networks. It therefore suggested that the fit obtained with gene PC1 was largely due to its spatial distribution on the cortical surface and not necessarily to its influence on pathogenic spreading processes unfolding on the structural connectome. For completeness, we also repeated these analyses in the three genetic subgroups of GENFI. Supplementary Fig. 6D shows that the results are consistent across subgroups, with *TARDBP* and *C9orf72* being the two gene distributions that give the largest model fits.

Discussion

The present report provides a comprehensive and statistically robust model supporting the theory of network-based atrophy in bvFTD, both in sporadic and genetic forms. Our findings are consistent across two datasets and the genetic/sporadic heterogeneity. Namely, for both sporadic and genetic variants, there is a strong correlation between node deformation and the mean of neighbour deformation defined by both structural and functional connectivity, supporting the theory that atrophy progresses through network-based connections. Similar findings were observed at small (219)

and large (1000) cortical parcellation resolutions. Data-driven epicentre mapping identified the bilateral anterior insular cortex as well as ventromedial cortex and antero-temporal areas as potential epicentres. The involvement of the antero-medial areas as epicentres ties into previous research showing that data-driven atrophy subtypes include a 'semantic appraisal network' predominant group.[13,74] The genetic bvFTD cohort showed a very similar profile of most likely epicentres, with the addition of some dorsal frontal areas. The role of these regions as epicentres was further supported by the agent-based spreading model.

The localization of cortical atrophy was most significant in the limbic resting state network and less present in the visuospatial network (expectedly given its posterior localization). There was significant atrophy in the default mode network (DMN) in genetic FTD, with a positive trend in sporadic FTD. Of note, the salience network, which has been previously identified as being predominantly involved in bvFTD,[10,11] did not show statistically significant atrophy. However, when looking at von Economo cytoarchitectonic classes, the insular cortex was the most affected, with relative sparing of the primary sensory neurons. This suggested that the insular cortex plays a central role in the disease, but not necessarily by spreading through the entire ventral attention network including its most posterior regions. In addition, while there have been some reports of opposite connectivity pattern of changes in the salience versus the DMN in bvFTD and Alzheimer's disease,[10] our results rather suggested that there is significant involvement of DMN regions in bvFTD.

Finally, although exploratory, using a simulation-based approach and gene expression profile data from the AHBA, we identified that the *C9orf72* and *TARDPB* gene expression could play a role in the propagation of atrophy in sporadic bvFTD. Indeed, factoring an impact on clearance and synthesis of both genes related to TDP-43 improved the fit between the spreading models and the actual atrophy maps based on DBM. While we cannot exclude that some subjects in the FTLDNI had an unidentified *C9orf72* mutation, the involvement of *TARDPB* is of interest given that mutations in this gene constitute only a very small fraction of genetic FTD. Results suggested that the activity of this gene could play a role in sporadic bvFTD, which could be of interest for future therapeutic avenues. Interestingly, we found that the atrophy in each of the three genetic groups in GENFI (*C9orf72*, *GRN*, *MAPT*) displayed a significant network spreading effect and overall has a similar dependence on local gene expression, but different network epicentres. Consistent with previous studies,[7] *C9orf72* and *MAPT* were marked by prominent epicentres in frontal, temporal and insular cortices that resemble sporadic cases, with more pronounced antero-medial temporal involvement in *MAPT*. *GRN*-related atrophy was marked by greater epicentre likelihood in more dorsal frontal areas and lateral parietal cortex. How population-level genetic variation shapes the molecular and network cascades that lead to atrophy remains an exciting question for future research.

It is important to note that these findings are mainly correlational and do not prove causal influence of network structure on atrophy. Specifically, it is not possible to determine whether connectivity drives the progression of grey matter atrophy or that connectome architecture itself is compromised in patients as a result of white-matter lesions reported in bvFTD, estimated by white matter hyperintensities.[75–78] We used structural and functional networks reconstructed from a sample of young healthy participants as the underlying architecture that supports pathogen transmission. However, extensive changes in network architecture may reroute or restrict the spread of pathology. It is also possible that white matter changes

disrupt normal transneuronal transport of trophic factors, resulting in atrophy among connected regions without involvement of any pathogens or misfolded proteins. These additional factors could be further investigated in more complex models using simultaneous measures of regional atrophy and changes in white matter architecture and structural and functional networks in a longitudinal sample of FTD patients. Specifically, a highly sampled, multimodal longitudinal dataset with simultaneous measurements of regional pathology, white-matter lesions, gene expression, metabolism, CSF biomarkers, vascular and neuroimaging factors in bvFTD would allow precise multifactorial modelling of the disease, improving individualized diagnosis, therapeutic interventions and prognosis in bvFTD patients.[79,80]

How could these results apply to individual patients? Because deformation-based morphometry is a technique intended to detect population-level differences in brain structure, we focused on group effects. Our findings provide a neurobiological explanation as to why patients with such different genetic and pathological variations can present with similar clinical syndromes in practice (i.e. because the disease propagation is constrained by the network architecture). Given the multifactorial nature of the disease and considerable inter-individual variability, it is necessary to tailor therapeutic interventions to individual patient needs. The central clinical promise of these network models is that they may effectively summarize the complex multimodal measurements available, yielding a small number of clinically relevant features. These features may then allow identification of at-risk pre-symptomatic individuals, candidates for enrollment in clinical trials and targets or outcome measures for novel disease modifying therapies.

Altogether, our results build on previous literature that patterns of neurodegeneration reflect network architecture.[14–18] Consistent with reports in other neurodegenerative diseases, we demonstrate that atrophy patterns in bvFTD are associated with global connectome architecture and local transcriptomic vulnerability.[9,11,19–26,37] The present findings were replicated in two separate samples of genetic and sporadic bvFTD and were validated using a range of methodological choices. We also confirmed that the findings are independent from potential confounding factors such as spatial distance and parcellation resolution. However, there are several methodological considerations that need to be taken into account when interpreting the findings.

First, there are currently no available molecular techniques to directly measure FTLD changes *in vivo*. To overcome this limitation, we opted to use DBM to estimate atrophy in bvFTD patients, since it is a robust method to capture local changes in brain tissue volume. Given that *in vivo* PET tracers of TDP-43 and tau PET tracers are not currently reliable in FTLD, using post-mortem assessments of pathology such as immunohistochemistry of phosphorylated TDP-43[81] would provide a more direct measure of FTD-related pathology.[82–84]

Second, we identified potential disease epicentres using cross sectional data and undirected networks, precluding reconstruction of the temporal sequence of pathology. In particular, the epicentre model cannot assess the cascade of pathology, including molecular, metabolic, vascular and functional changes, that may begin before grey matter atrophy and start years before emergence of the clinical syndromes and disease diagnosis.[85] Modelling disease progression and spread of atrophy across brain networks over time remains an exciting open question that could eventually be addressed by increased longitudinal sampling in large FTD datasets (including GENFI and

ALLFTD[86,87]) that include multimodal data from presymptomatic genetic carriers to symptomatic patients at later stages of diseases.

Third, DSI and streamline tractography were used to estimate structural connectivity networks. Although recent technological and analytical developments provide powerful methods to reconstruct white matter fibers *in vivo*, with biologically interpretable weights and good correspondence with histology, they may still yield false positives and negatives.[88–96] Fourth, the two multi-site datasets included in this study have different demographics that could potentially influence the results. Although the morphometric procedure controls for site, age and sex, and the results are consistent across the two datasets, our findings should be interpreted in light of these potential confounding variables.[97,98]

Conclusion

Altogether, structural and functional connectivity networks and rigorous statistical analyses that account for spatial autocorrelation and network embedding were used in the present study to demonstrate that bvFTD-related neurodegeneration is conditioned by connectome architecture, accounting for 30–40% of variance in atrophy as well as local transcriptomic vulnerability. FTD-related atrophy appears to target particular regions associated with the anterior insular cortex, but it is likely that there are multiple potential epicentres leading to bvFTD clinical phenotypes. The similarity between genetic and sporadic forms of bvFTD suggests that multiple pathological changes are constrained by the network architecture in the spread of atrophy, explaining why many different pathological and genetic entities lead to the same clinical syndrome. Although exploratory, our results suggest that *TARDPB* gene expression could have a significant contribution to disease progression, particularly in sporadic bvFTD.

Acknowledgements

Funding

Competing interests

The authors report no competing interests.

Supplementary material

Supplementary material is available at *Brain* online.

Appendix 1

Further details of the FTLDNI investigators and GENFI consortium members are provided in the Supplementary material.

FTLDNI investigators

Howard Rosen, Bradford C. Dickerson, Kimoko Domoto-Reilly, David Knopman, Bradley F. Boeve, Adam L. Boxer, John Kornak, Bruce L. Miller, William W. Seeley, Maria-Luisa Gorno-Tempini, Scott McGinnis, Maria Luisa Mandelli.

GENFI consortium members

Aitana Sogorb Esteve, Annabel Nelson, Arabella Bouzigues, Carolin Heller, Caroline V. Greaves, David Cash, David L. Thomas, Emily Todd, Hanya Benotmane, Henrik Zetterberg, Imogen J. Swift, Jennifer Nicholas, Kiran Samra, Lucy L. Russell, Martina Bocchetta, Rachelle Shafei, Rhian S. Convery, Carolyn Timberlake, Thomas Cope, Timothy Rittman, Alberto Benussi, Enrico Premi, Roberto Gasparotti, Silvana Archetti, Stefano Gazzina, Valentina Cantoni, Andrea Arighi, Chiara Fenoglio, Elio Scarpini, Giorgio Fumagalli, Vittoria Borracci, Giacomina Rossi, Giorgio Giaccone, Giuseppe Di Fede, Paola Caroppo, Pietro Tiraboschi, Sara Prioni, Veronica Redaelli, David Tang-Wai, Ekaterina Rogaeva, Miguel Castelo-Branco, Morris Freedman, Ron Keren, Sandra Black, Sara Mitchell, Christen Shoesmith, Robart Bartha, Rosa Rademakers, Emma van der Ende, Jackie Poos, Janne M. Papma, Lucia Giannini, Rick van Minkelen, Yolande Pijnenburg, Benedetta Nacmias, Camilla Ferrari, Cristina Polito, Gemma Lombardi, Valentina Bessi, Michele Veldsman, Christin Andersson, Hakan Thonberg, Linn Öijerstedt, Vesna Jelic, Paul Thompson, Tobias Langheinrich, Albert Lladó, Anna Antonell, Jaume Olives, Mircea Balasa, Nuria Bargalló, Sergi Borrego-Ecija, Ana Verdelho, Carolina Maruta, Catarina B. Ferreira, Gabriel Miltenberger, Frederico Simões do Couto, Alazne Gabilondo, Ana Gorostidi, Jorge Villanua, Marta Cañada, Mikel Tainta, Miren Zulaica, Myriam Barandiaran, Patricia Alves, Benjamin Bender, Carlo Wilke, Lisa Graf, Annick Vogels, Mathieu Vandenbulcke, Philip Van Damme, Rose Bruffaerts, Pedro Rosa-Neto, Serge Gauthier, Agnès Camuzat, Alexis Brice, Anne Bertrand, Aurélie Funkiewiez, Daisy Rinaldi, Dario Saracino, Olivier Colliot, Sabrina Sayah, Catharina Prix, Elisabeth Wlasich, Olivia Wagemann, Sandra Loosli, Sonja Schönecker, Tobias Hoegen, Jolina Lombardi, Sarah Anderl-Straub, Adeline Rollin, Gregory Kuchcinski, Maxime Bertoux, Thibaud Lebouvier, Vincent Deramecourt, Beatriz Santiago, Diana Duro, Maria João Leitão, Maria Rosario Almeida, Miguel Tábuas-Pereira, Sónia Afonso, Annerose Engel, Maryna Polyakova.

References

1. Ratnavalli E, Brayne C, Dawson K, Hodges JR. The prevalence of frontotemporal dementia. *Neurology*. 2002;58(11):1615–1621.

2. Onyike CU, Diehl-Schmid J. The epidemiology of frontotemporal dementia. *Int Rev Psychiatry*. 2013;25(2):130–137.

3. Rascovsky K, Hodges JR, Knopman D, *et al.* Sensitivity of revised diagnostic criteria for the behavioural variant of frontotemporal dementia. *Brain*. 2011;134(9):2456–2477.

4. Rademakers R, Neumann M, Mackenzie IR. Advances in understanding the molecular basis of frontotemporal dementia. *Nat Rev Neurol*. 2012;8(8):423–434.

5. Meeter LH, Kaat LD, Rohrer JD, van Swieten JC. Imaging and fluid biomarkers in frontotemporal dementia. *Nat Rev Neurol*. 2017;13(7):406–419.

6. Ducharme S, Dols A, Laforce R, *et al.* Recommendations to distinguish behavioural variant frontotemporal dementia from psychiatric disorders. *Brain*. 2020;143(6):1632–1650.

7. Cash DM, Bocchetta M, Thomas DL, *et al.* Patterns of gray matter atrophy in genetic frontotemporal dementia: Results from the GENFI study. *Neurobiol Aging*. 2018;62:191–196.

8. Seeley WW. Mapping neurodegenerative disease onset and progression. *Cold Spring Harb Perspect Biol*. 2017;9(8):a023622.

9. Zhou J, Gennatas ED, Kramer JH, Miller BL, Seeley WW. Predicting regional neurodegeneration from the healthy brain functional connectome. *Neuron*. 2012;73(6):1216–1227.

10. Zhou J, Greicius MD, Gennatas ED, *et al.* Divergent network connectivity changes in behavioural variant frontotemporal dementia and Alzheimer's disease. *Brain*. 2010;133(5):1352–1367.

11. Seeley WW, Zhou J, Kim EJ. Frontotemporal dementia: What can the behavioral variant teach us about human brain organization? *Neuroscientist*. 2012;18(4):373–385.

12. Kim EJ, Sidhu M, Gaus SE, *et al.* Selective frontoinsular von economo neuron and fork cell loss in early behavioral variant frontotemporal dementia. *Cereb Cortex*. 2016;26(4):1843.

13. Ranasinghe KG, Rankin KP, Pressman PS, *et al.* Distinct subtypes of behavioral variant frontotemporal dementia based on patterns of network degeneration. *JAMA Neurol*. 2016;73(9):1078–1088.

14. Fornito A, Zalesky A, Breakspear M. The connectomics of brain disorders. *Nat Rev Neurosci*. 2015;16(3):159–172.

15. Jucker M, Walker LC. Self-propagation of pathogenic protein aggregates in neurodegenerative diseases. *Nature*. 2013;501(7465):45–51.

16. Warren JD, Rohrer JD, Hardy J. Disintegrating brain networks: From syndromes to molecular nexopathies. *Neuron*. 2012;73(6):1060–1062.

17. Warren JD, Rohrer JD, Schott JM, Fox NC, Hardy J, Rossor MN. Molecular nexopathies: A new paradigm of neurodegenerative disease. *Trends Neurosci*. 2013;36(10):561–569.

18. Raj A, Powell F. Models of network spread and network degeneration in brain disorders. *Biol Psychiatry Cogn Neurosci Neuroimaging*. 2018;3(9):788–797.

19. Carbonell F, Iturria-Medina Y, Evans AC. Mathematical modeling of protein misfolding mechanisms in neurological diseases: A historical overview. *Front Neurol*. 2018;9:37.

20. Polymenidou M, Cleveland DW. The seeds of neurodegeneration: Prion-like spreading in ALS. *Cell*. 2011;147(3):498–508.

21. Raj A. Graph models of pathology spread in Alzheimer's disease: An alternative to conventional graph theoretic analysis. *Brain Connect*. 2021;11(10):799–814.

22. Raj A, Kuceyeski A, Weiner M. A network diffusion model of disease progression in dementia. *Neuron*. 2012;73(6):1204–1215.

23. Brandner S, Jaunmuktane Z. Prion disease: Experimental models and reality. *Acta Neuropathol*. 2017;133(2):197–222.

24. Fornari S, Schäfer A, Jucker M, Goriely A, Kuhl E. Prion-like spreading of Alzheimer's disease within the brain's connectome. *J R Soc Interface*. 2019;16(159):20190356.

25. Weickenmeier J, Jucker M, Goriely A, Kuhl E. A physics-based model explains the prion-like features of neurodegeneration in Alzheimer's disease, Parkinson's disease, and amyotrophic lateral sclerosis. *J Mech Phys Solids*. 2019;124:264–281.

26. Meier JM, van der Burgh HK, Nitert AD, *et al.* Connectome-based propagation model in amyotrophic lateral sclerosis. *Ann Neurol*. 2020;87(5):725–738.

27. Peng C, Trojanowski JQ, Lee VM-Y. Protein transmission in neurodegenerative disease. *Nat Rev Neurol*. 2020;16(4):199–212.

28. Kim EJ, Hwang JL, Gaus SE, *et al.* Evidence of corticofugal tau spreading in patients with frontotemporal dementia. *Acta Neuropathol*. 2020;139(1):27–43.

29. Brown JA, Deng J, Neuhaus J, *et al.* Patient-tailored, connectivity-based forecasts of spreading brain atrophy. *Neuron*. 2019;104(5):856–868.e5.

30. Suarez LE, Markello RD, Betzel RF, Misic B. Linking structure and function in macroscale brain networks. *Trends Cogn Sci*. 2020;24(4):302–315.

31. Schmidt R, de Reus MA, Scholtens LH, van den Berg LH, van den Heuvel MP. Simulating disease propagation across white matter connectome reveals anatomical substrate for neuropathology staging in amyotrophic lateral sclerosis. *Neuroimage*. 2016;124(Pt A):762–769.

32. Kassubek J, Muller HP, Del Tredici K, *et al.* Longitudinal diffusion tensor imaging resembles patterns of pathology progression in behavioral variant frontotemporal dementia (bvFTD). *Front Aging Neurosci*. 2018;10:47.

33. Kassubek J, Müller HP, Del Tredici K, *et al.* Imaging the pathoanatomy of amyotrophic lateral sclerosis in vivo: Targeting a propagation-based biological marker. *J Neurol Neurosurg Psychiatry*. 2018;89(4):374–381.

34. Zheng YQ, Zhang Y, Yau Y, *et al.* Local vulnerability and global connectivity jointly shape neurodegenerative disease propagation. *PLoS Biol*. 2019;17(11):e3000495.

35. Freeze B, Acosta D, Pandya S, Zhao Y, Raj A. Regional expression of genes mediating trans-synaptic alpha-synuclein transfer predicts regional atrophy in Parkinson disease. *Neuroimage Clin*. 2018;18:456–466.

36. Raj A, Powell F. Network model of pathology spread recapitulates neurodegeneration and selective vulnerability in Huntington's disease. *Neuroimage*. 2021;235:118008.

37. Zeighami Y, Ulla M, Iturria-Medina Y, *et al.* Network structure of brain atrophy in de novo Parkinson's disease. *Elife*. 2015;4:e08440.

38. Rohrer JD, Nicholas JM, Cash DM, *et al.* Presymptomatic cognitive and neuroanatomical changes in genetic frontotemporal dementia in the Genetic Frontotemporal dementia Initiative (GENFI) study: A cross-sectional analysis. *Lancet Neurol*. 2015;14(3):253–262.

39. Aubert-Broche B, Fonov VS, Garcia-Lorenzo D, *et al.* A new method for structural volume analysis of longitudinal brain MRI data and its application in studying the growth trajectories of anatomical brain structures in childhood. *Neuroimage*. 2013;82:393–402.

40. Coupe P, Yger P, Prima S, Hellier P, Kervrann C, Barillot C. An optimized blockwise nonlocal means denoising filter for 3-D magnetic resonance images. *IEEE Trans Med Imaging*. 2008;27(4):425–441.

41. Sled JG, Zijdenbos AP, Evans AC. A nonparametric method for automatic correction of intensity nonuniformity in MRI data. *IEEE Trans Med Imaging*. 1998;17(1):87–97.

42. Collins DL, Neelin P, Peters TM, Evans AC. Automatic 3D inter-subject registration of MR volumetric data in standardized Talairach space. *J Comput Assist Tomogr*. 1994;18(2):192–205.

43. Dadar M, Fonov VS, Collins DL. A comparison of publicly available linear MRI stereotaxic registration techniques. *Neuroimage*. 2018;174:191–200.

44. Dadar M, Maranzano J, Ducharme S, Collins DL. White matter in different regions evolves differently during progression to dementia. *Neurobiol Aging*. 2019;76:71–79.

45. Boucetta S, Salimi A, Dadar M, Jones BE, Collins DL, Dang-Vu TT. Structural brain alterations associated with rapid eye movement sleep behavior disorder in Parkinson's disease. *Sci Rep*. 2016;6:26782.

46. Avants BB, Epstein CL, Grossman M, Gee JC. Symmetric diffeomorphic image registration with cross-correlation: evaluating automated labeling of elderly and neurodegenerative brain. *Med Image Anal*. 2008;12(1):26–41.

47. Ashburner J, Friston KJ. Voxel-based morphometry–the methods. *Neuroimage*. 2000;11(6 Pt 1):805–821.

48. Ashburner J, Hutton C, Frackowiak R, Johnsrude I, Price C, Friston K. Identifying global anatomical differences: Deformation-based morphometry. *Hum Brain Mapp*. 1998;6-(5-6):348–57.

49. Manera AL, Dadar M, Collins DL, Ducharme S. Deformation based morphometry study of longitudinal MRI changes in behavioral variant frontotemporal dementia. *Neuroimage Clin*. 2019;24:102079.

50. Cammoun L, Gigandet X, Meskaldji D, *et al*. Mapping the human connectome at multiple scales with diffusion spectrum MRI. *J Neurosci Methods*. 2012;203(2):386–397.

51. Desikan RS, Segonne F, Fischl B, *et al*. An automated labeling system for subdividing the human cerebral cortex on MRI scans into gyral based regions of interest. *Neuroimage*. 2006;31(3):968–980.

52. Griffa A, Alemán-Gómez Y, Hagmann P. Structural and functional connectome from 70 young healthy adults. *Zenodo*. 2019.

53. Betzel RF, Griffa A, Hagmann P, Mišić B. Distance-dependent consensus thresholds for generating group-representative structural brain networks. *Netw Neurosci*. 2019;3(2):475–496.

54. Mišić B, Betzel RF, Nematzadeh A, *et al*. Cooperative and competitive spreading dynamics on the human connectome. *Neuron*. 2015;86(6):1518–1529.

55. Misic B, Betzel RF, Griffa A, *et al*. Network-based asymmetry of the human auditory system. *Cereb Cortex*. 2018;28:2655–2664.

56. Shafiei G, Markello RD, Makowski C, *et al*. Spatial patterning of tissue volume loss in schizophrenia reflects brain network architecture. *Biol Psychiatry*. 2020;87(8):727–735.

57. Vazquez-Rodríguez B, Suárez LE, Markello RD, *et al*. Gradients of structure-function tethering across neocortex. *Proc Natl Acad Sci USA*. 2019;116(42):21219–21227.

58. Hawrylycz MJ, Lein ES, Guillozet-Bongaarts AL, *et al*. An anatomically comprehensive atlas of the adult human brain transcriptome. *Nature*. 2012;489(7416):391–399.

59. Burt JB, Demirtas M, Eckner WJ, *et al*. Hierarchy of transcriptomic specialization across human cortex captured by structural neuroimaging topography. *Nat Neurosci*. 2018;21(9):1251–1259.

60. Markello RD, Arnatkevičiūté A, Poline J-B, Fulcher BD, Fornito A, Misic B. Standardizing workflows in imaging transcriptomics with the abagen toolbox. *Elife*. 2021;10:e72129.

61. Arnatkevičiūté A, Fulcher BD, Fornito AJN. A practical guide to linking brain-wide gene expression and neuroimaging data. *NeuroImage*. 2019;189:353–367.

62. Fulcher BD, Fornito A. A transcriptional signature of hub connectivity in the mouse connectome. *Proc Natl Acad Sci USA* 2016;113(5):1435–1440.

63. Alexander-Bloch AF, Shou H, Liu S, *et al*. On testing for spatial correspondence between maps of human brain structure and function. *Neuroimage* 2018;178:540–551.

64. Markello RD, Misic B. Comparing spatial null models for brain maps. *Neuroimage* 2021;236:118052.

65. Daducci A, Gerhard S, Griffa A, *et al*. The connectome mapper: An open-source processing pipeline to map connectomes with MRI. *PLoS One*. 2012;7(12):e48121.

66. Burt JB, Helmer M, Shinn M, Anticevic A, Murray JD. Generative modeling of brain maps with spatial autocorrelation. *Neuroimage*. 2020;220:117038.

67. Betzel RF, Bassett DS. Specificity and robustness of long-distance connections in weighted, interareal connectomes. *Proc Natl Acad Sci USA*. 2018;115(21):E4880–E4889.

68. Yeo BT, Krienen FM, Sepulcre J, *et al*. The organization of the human cerebral cortex estimated by intrinsic functional connectivity. *J Neurophysiol*. 2011;106(3):1125–1165.

69. von Economo CF, Koskinas GN. *Die cytoarchitektonik der hirnrinde des erwachsenen menschen*. J. Springer; 1925.

70. Scholtens LH, de Reus MA, de Lange SC, Schmidt R, van den Heuvel MP. An MRI Von Economo - Koskinas atlas. *Neuroimage*. 2018;170:249–256.

71. Váša F, Seidlitz J, Romero-Garcia R, *et al*. Adolescent tuning of association cortex in human structural brain networks. *Cereb Cortex*. 2018;28(1):281–294.

72. Vértes PE, Rittman T, Whitaker KJ, *et al*. Gene transcription profiles associated with inter-modular hubs and connection distance in human functional magnetic resonance imaging networks. *Philos Trans R Soc Lond B Biol Sci*. 2016;371(1705):20150362.

73. Greaves CV, Rohrer JD. An update on genetic frontotemporal dementia. *J Neurol*. 2019;266(8):2075–2086.

74. Guo CC, Gorno-Tempini ML, Gesierich B, *et al*. Anterior temporal lobe degeneration produces widespread network-driven dysfunction. *Brain*. 2013;136(Pt 10):2979–2991.

75. Caroppo P, Le Ber I, Camuzat A, *et al*. Extensive white matter involvement in patients with frontotemporal lobar degeneration: Think progranulin. *JAMA Neurol*. 2014;71(12):1562–1566.

76. Paternico D, Premi E, Gazzina S, *et al*. White matter hyperintensities characterize monogenic frontotemporal dementia with granulin mutations. *Neurobiol Aging*. 2016;38:176–180.

77. Sudre CH, Bocchetta M, Cash D, *et al*. White matter hyperintensities are seen only in GRN mutation carriers in the GENFI cohort. *Neuroimage Clin*. 2017;15:171–180.

78. Dadar M, Manera A, Ducharme S, Collins DL. White matter hyperintensities are associated with grey matter atrophy and cognitive decline in Alzheimer's disease and frontotemporal dementia. *Neurobiol Aging*. 2022;111:54–63.

79. Iturria-Medina Y, Carbonell FM, Evans AC, Alzheimer's Disease Neuroimaging Initiative. Multimodal imaging-based therapeutic fingerprints for optimizing personalized interventions: Application to neurodegeneration. *Neuroimage*. 2018;179:40–50.

80. Iturria-Medina Y, Carbonell FM, Sotero RC, Chouinard-Decorte F, Evans AC, Alzheimer's Disease Neuroimaging Initiative. Multifactorial causal model of brain (dis)organization and therapeutic intervention: Application to Alzheimer's disease. *Neuroimage*. 2017;152:60–77.

81. Brettschneider J, Del Tredici K, Irwin DJ, *et al*. Sequential distribution of pTDP-43 pathology in behavioral variant frontotemporal dementia (bvFTD). *Acta Neuropathol*. 2014;127(3):423–439.

82. Mackenzie IR, Neumann M. Molecular neuropathology of frontotemporal dementia: Insights into disease mechanisms from postmortem studies. *J Neurochem.* 2016;138(Suppl 1):54–70.

83. Hall B, Mak E, Cervenka S, Aigbirhio FI, Rowe JB, O'Brien JT. In vivo tau PET imaging in dementia: Pathophysiology, radiotracer quantification, and a systematic review of clinical findings. *Ageing Res Rev.* 2017;36:50–63.

84. Fleisher AS, Pontecorvo MJ, Devous MD Sr, *et al.* Positron emission tomography imaging with [18F]flortaucipir and postmortem assessment of Alzheimer disease neuropathologic changes. *JAMA Neurol.* 2020;77(7):829–839.

85. van der Ende EL, Bron EE, Poos JM, *et al.* A data-driven disease progression model of fluid biomarkers in genetic frontotemporal dementia. *Brain.* 2021;145(5):1805–1817.

86. Boeve B, Bove J, Brannelly P, *et al.* The longitudinal evaluation of familial frontotemporal dementia subjects protocol: Framework and methodology. *Alzheimers Dement.* 2020;16(1):22–36.

87. Rosen HJ, Boeve BF, Boxer AL. Tracking disease progression in familial and sporadic frontotemporal lobar degeneration: Recent findings from ARTFL and LEFFTDS. *Alzheimers Dement.* 2020;16(1):71–78.

88. Thomas C, Ye FQ, Irfanoglu MO, *et al.* Anatomical accuracy of brain connections derived from diffusion MRI tractography is inherently limited. *Proc Natl Acad Sci USA.* 2014;111(46):16574–16579.

89. Jbabdi S, Sotiropoulos SN, Haber SN, Van Essen DC, Behrens TE. Measuring macroscopic brain connections in vivo. *Nat Neurosci.* 2015;18(11):1546–1555.

90. Donahue CJ, Sotiropoulos SN, Jbabdi S, *et al.* Using diffusion tractography to predict cortical connection strength and distance: A quantitative comparison with tracers in the monkey. *J Neurosci.* 2016;36(25):6758–6770.

91. Maier-Hein KH, Neher PF, Houde JC, *et al.* The challenge of mapping the human connectome based on diffusion tractography. *Nat Commun.* 2017;8(1):1349.

92. Schilling KG, Nath V, Hansen C, *et al.* Limits to anatomical accuracy of diffusion tractography using modern approaches. *Neuroimage.* 2019;185:1–11.

93. Shen K, Goulas A, Grayson DS, *et al.* Exploring the limits of network topology estimation using diffusion-based tractography and tracer studies in the macaque cortex. *Neuroimage.* 2019; 191:81–92.

94. Sotiropoulos SN, Zalesky A. Building connectomes using diffusion MRI: Why, how and but. *NMR Biomed.* 2019;32(4):e3752.

95. Boshkovski T, Kocarev L, Cohen-Adad J, *et al.* The R1-weighted connectome: Complementing brain networks with a myelin-sensitive measure. *Netw Neurosci.* 2021;5(2):358–372.

96. Dhollander T, Clemente A, Singh M, *et al.* Fixel-based analysis of diffusion MRI: methods, applications, challenges and opportunities. *Neuroimage.* 2021;241:118417.

97. Fortin JP, Cullen N, Sheline YI, *et al.* Harmonization of cortical thickness measurements across scanners and sites. *Neuroimage.* 2018;167:104–120.

98. Eshaghzadeh Torbati M, Minhas DS, Ahmad G, *et al.* A multi-scanner neuroimaging data harmonization using RAVEL and ComBat. *Neuroimage.* 2021;245:118703.